Elimination of imaging artifacts in second harmonic generation microscopy using interferometry

Maxime Pinsard, Margaux Schmeltz, Jarno van Der Kolk, Shunmoogum A. Patten, Heide Ibrahim, Lora Ramunno, Marie-Claire Schanne-Klein, François Légaré

Research Article | Vol. 10, No. 8 | 1 Aug 2019 | BIOMEDICAL OPTICS EXPRESS 3938
Biomedical Optics EXPRESS

Elimination of imaging artifacts in second harmonic generation microscopy using interferometry

MAXIME PINSARD,[1] MARGAUX SCHMELTZ,[2] JARNO VAN DER KOLK,[3] SHUNMOOGUM A PATTEN,[4] HEIDE IBRAHIM,[1] LORA RAMUNNO,[3] MARIE-CLAIRE SCHANNE-KLEIN,[2] AND FRANÇOIS LÉGARÉ[1,*]

[1]*Institut National de la Recherche Scientifique, Centre Énergie Matériaux Télécommunications (INRS-EMT); 1650 Boul. Lionel-Boulet, Varennes (QC), J3X 1S2, Canada*
[2]*Laboratoire d'Optique et Biosciences (LOB), École Polytechnique, CNRS, Inserm, Institut Polytechnique de Paris, F-91128 Palaiseau, France*
[3]*Department of Physics and Centre for Research in Photonics, University of Ottawa, Ottawa (ON), K1N 6N5, Canada*
[4]*INRS-Institut Armand-Frappier, Laval, Québec, Canada, H7V 1B7, Canada*
[*]*legare@emt.inrs.ca*

Abstract: Conventional second harmonic generation (SHG) microscopy might not clearly reveal the structure of complex samples if the interference between all scatterers in the focal volume results in artefactual patterns. We report here the use of interferometric second harmonic generation (I-SHG) microscopy to efficiently remove these artifacts from SHG images. Interfaces between two regions of opposite polarity are considered because they are known to produce imaging artifacts in muscle for instance. As a model system, such interfaces are first studied in periodically-poled lithium niobate (PPLN), where an artefactual incoherent SH signal is obtained because of irregularities at the interfaces, that overshadow the sought-after coherent contribution. Using I-SHG allows to remove the incoherent part completely without any spatial filtering. Second, I-SHG is also proven to resolve the double-band pattern expected in muscle where standard SHG exhibits in some regions artefactual single-band patterns. In addition to removing the artifacts at the interfaces between antiparallel domains in both structures (PPLN and muscle), I-SHG also increases their visibility by up to a factor of 5. This demonstrates that I-SHG is a powerful technique to image biological samples at enhanced contrast while suppressing artifacts.

1. Introduction

Over the last 30 years, Second Harmonic Generation (SHG) microscopy has been gradually confirmed as a powerful tool for high contrast imaging of structures that lack centrosymmetry, in particular some specific biological structures [1–3]. This parametric process generates a single photon at twice the frequency of two incident photons. This, as a multiphoton process, provides the benefit of confining the excitation in the focal volume thus providing intrinsic sub-micron spatial resolution [4]. Furthermore, the use of a near-infrared laser reduces the negative impact of tissue scattering, providing deep-tissue imaging [5]. The SHG signal also scales quadratically with the number of aligned molecules for structures smaller than the focal volume [6,7], and is free of energy losses as no electron is transferred. This considerably reduces phototoxicity and avoids photobleaching [8]. Given its high specificity for non-centrosymmetric media [9], this technique is widely used as a very sensitive and specific structural probe of various biopolymers such as tendon [10,11], cartilage [12], skeletal muscle [13,14] or mitotic spindles [15]. Importantly, this process preserves the coherence of the laser light (spatial and temporal) [6] and is thus able to convey information on the polarity of the scatterers [16,17]. Even though this information is

#363834 https://doi.org/10.1364/BOE.10.003938
Journal © 2019 Received 1 Apr 2019; revised 17 Jun 2019; accepted 17 Jun 2019; published 12 Jul 2019

Biomedical Optics EXPRESS

preserved in conventional SHG microscopy, it requires the interferometric-SHG (I-SHG) method to read it out. I-SHG indeed allows to measure the relative phase of SHG signals from different structures in the sample, and thus to map their relative polarity. It was first applied to non-centrosymmetric crystals [18] and later to biological tissues like muscle [19]. Having revealed the heterogeneous distribution of bundles of fibers in tendon [20], this technique was then used in articular cartilage to discriminate, in zones with low SHG signal, the spots with a random organization of fibrils from those with bundles of fibrils of opposite polarity [21]. Recently, the polarity of microtubules during mitosis was measured [22] after a technological development to increase the speed of the measurement [23]. In this manuscript, we will refer to I-SHG for Interferometric-SHG and to standard or conventional SHG for intensity SHG.

In conventional SHG microscopy, the imaged features are always the result of complex interferences between scatterers exhibiting a non-zero $\chi^{(2)}$, where $\chi^{(2)}$ is the uniform second-order nonlinear optical susceptibility coefficient involved in the interaction that acts as an SHG converter (see [24] for its definition). While these interferences can be seen as a direct link to the real structure in rather simple cases like tail tendon, other patterns are considered as artifacts as the real organization of $\chi^{(2)}$ scatterers is difficult to extract [25,26].

In periodically-poled $LiNbO_3$ crystals (PPLN), there is a periodic alternation of domains of opposite polarity (see Fig. 1(A)). This material is known to have crystal lattice distortions [27], frustration, and defects close to the domain walls [28,29], where the polarity inverts between two homogeneous domains. This leads to a non-negligible change in polarization [28] and refractive index inhomogeneities in this region, which causes light scattering and distortion of the wavefront [30,31].

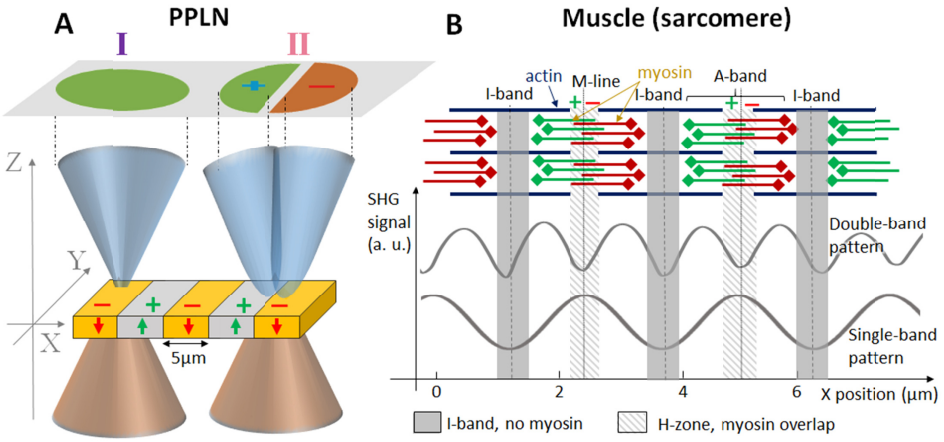

Fig. 1. Schematic structures of Periodically-Poled Lithium Niobate (PPLN, A) and myosin (B), both showing an alternation of domains of opposite polarity. (A) When being imaged by SHG, the excitation beam can be focused inside one PPLN domain (in the bulk, I) or at the interface between two domains (II) leading to a change of the emitted SHG radiation pattern depicted at the top. (B) Structure of myosin inside the sarcomeres of muscles, which consist of A-bands of myosin separated by I-bands (with no myosin). Some thin actin filaments also alternate with certain spacing at the H-zone, located in the middle of the A-band. The symmetry and bipolarity of the myosin filaments lead to alternating maximum and minimum SHG signal, which has two origins. The dips corresponding to the large I-band (dark grey in B)) are always visible because of a lack of myosin (single-band pattern), so no SHG. In addition, the proximity of myosin ends of opposite polarity at the M-line (striped light grey in B)) should lead to measured destructive interferences from π phase-shifted SHG signals, and thus the observation of twice the number of minima, that is the double-band pattern. However, these are sometimes not observed in SHG microscopy.

Skeletal muscles are to some extent similar to PPLN as they also feature an alternation of domains of opposite polarity [19]: the myosin filaments are well-organized inside the sarcomeres with a specific structure depicted in Fig. 1(B)). They are present only in the A-

Biomedical Optics EXPRESS

band, and precisely at its center (called the H-zone or M-line), where the ends of the filaments of opposite polarity overlap. This leads to SHG signals of opposite amplitude (their phase are π phase-shifted). Between two A-bands of myosin is the I-band located, which contains no myosin and therefore does not contribute to the SHG signal. This is well illustrated by the alternation of dips in the SHG signal when imaging the sarcomeres [32,33] and refers to as a single-band pattern (see Fig. 1(B)). However, because some destructive interferences should occur for the signal collected at the M-line, there should be another dip at this position which is indeed observed in some cases [33,34] and is called a double-band pattern (see Fig. 1(B)). This so-called SHG "vernier" has already been observed [33,35,36] and was linked to the proteolysis state of the muscle [32]. Other studies have postulated an effect of damage reparation [36].

While the physical increase of the separation of the two ends of the myosin filaments theoretically leads to a decrease or even the disappearance of the SHG dip at this interface, recent studies state that the single-band pattern originates most of the time from imaging artifacts, which are the result of interferences (and thus of the coherent nature of the SHG light) between adjacent myofibers [25,26].

In this work, we show that SHG artifacts at the interface can have two different origins, either incoherent in the case of PPLN, or coherent for myosin. A strong and scattered second-harmonic signal arises from the nonlinear interaction at the interfaces of the domains in PPLN, which is an artifact since it produces a very high second-harmonic signal that overshadows the real structure. Most of this signal is shown to be eliminated through I-SHG measurements, as it only contributes to the background due to its incoherent nature. We also show that this technique removes the artifacts leading to single-band patterns in muscle, and thus reveals the true nature of the sarcomeres when being imaged by SHG. We show in addition that I-SHG allows to increase the visibility of those interfaces compared to conventional SHG.

2. Materials and methods

2.1 SHG and I-SHG microscopy

For a complete description of the I-SHG method and SHG set-up we refer to [23]. Importantly, an air immersion objective (UplanSApo 20X, NA 0.75, Olympus, Japan)) was used for excitation and the SHG emission was then collected with a 0.8NA objective (LUMPlanFLN, 40X, Olympus) to ensure that the numerical aperture is sufficiently high to collect the whole radiation pattern. The (measured) focal volume of excitation is then of $1x1x4\mu m^3$: the deviation from the theoretical values ($0.4x0.4x1.9\mu m^3$, see [37]) comes from an imperfect collimation and underfilling of the back pupil of the objective, as well as reduced performances from the objective lens. Scanning and signal acquisition were synchronized using a custom-written Python (www.python.org) program for better stability and control.

Standard SHG frames were recorded in the forward direction, in ~3 s, using 20 µs pixel dwell-time and 100 nm pixel size in order to oversample the structure. The average power on the sample was adjusted to 15mW, corresponding to 0.2 nJ/pulse. Raw data visualization was performed with FIJI-ImageJ (NIH [38]) and image processing with MATLAB.

Moreover, a circular iris whose aperture can be gradually decreased down to 5mm diameter was inserted after the collecting objective to allow optional rejection of selected scattered parts of the converted SHG.

2.2 Interferometric contrast and phase in I-SHG

In I-SHG, the phase information is extracted from the interference between the SH generated in the sample and a reference SH beam. The intensity measured at pixel i on an interferogram at phase-shift δ_j can be written as [39,40]:

Biomedical Optics EXPRESS

$$I_i(\delta_j) = A_{ij} + B_{ij} sinc(\Delta/2)\cos(\phi_i + \delta_j) \quad (1)$$

Each interferogram at phase-shift δ_j is subtracted from the one at phase-shift $\delta_j + \pi$:

$$I_i(\delta_j + \pi) - I_i(\delta_j) = 2B_{ij} sinc(\Delta/2)\cos(\phi_i + \delta_j) = b_i \cos(\delta_j) + c_i \sin(\delta_j) \quad (2)$$

where:

$$\begin{aligned} b_i &= 2B_{ij} sinc(\Delta/2)\cos(\phi_i) \\ c_i &= -2B_{ij} sinc(\Delta/2)\sin(\phi_i) \end{aligned} \quad (3)$$

ϕ_i being the relative phase at pixel i. Δ is the integration range of time where the phase-shift varies linearly, which is here zero because the phase-shift is changed by discrete steps and not continuously ($sinc(\Delta/2) = 1$). a_i, b_i and c_i are assumed to be independent on phase-shift variations (i.e. of j), and to only be functions of the pixel position in the image (i.e. of i) [40]. This is usually justified if the laser intensity is maintained constant for all the measurements [39]. The interferometric contrast is then $\gamma_i = \sqrt{b_i^2 + c_i^2}$, where b_i (resp. c_i) is fitted over all δ_j (i.e. the different phase-shifts) for every pixel i. I-SHG allows to measure both the phase ϕ_i and the interferometric contrast γ_i. Similarly, the relative phase ϕ_i can be expressed as: $\tan\phi_i = c_i / b_i$, and is extracted in [–π, π] using the 2-arguments Arctangent function. The real phase-shift induced by the phase-shifter (a rotating glass plate) is non-linear with the glass plate angle and must be first calibrated (see [41]). Also, because the reference and excitation waves both scan the sample by passing through the excitation objective, their retardation varies differently during the scan and some aberrations inevitably appear. A reference correction (as described in [42]) is then applied to the phase and contrast maps to correct it. For more details see [23].

2.3 Periodically-poled lithium niobate (PPLN)

The PPLN is a quasi-phase matching rectangular crystal for SHG conversion at 1064nm (MSHG1064-0.5-xx PPLN, Covesion) with dimensions 10x0.5x0.5mm^3. It consists of a LiNbO3 crystal with a succession of domains of opposite polarity engraved by high voltage. The crystal is imaged in a plane orthogonal to the axis that is normally used for quasi-phase matching (see Fig. 1(A)) by placing it on a microscope coverslip #1.5H (Thorlabs).

2.4 Skeletal muscle – sample preparation

Wild-type zebrafish (*Danio rerio*) of the TL (*Tupfel long fin*) line were bred and maintained according to standard procedure [43]. All experiments were performed in compliance with the guidelines of the Canadian Council for Animal Care and our local animal care committee. Zebrafish (6-months old) and larvae (3 days postfertilization) were fixed in 4% paraformaldehyde. The muscles from 6-months old zebrafish were embedded in paraffin. Sections (6 µm) of paraffin-embedded specimens were deparaffinized in xylene and rehydrated in a graded series of ethanol solutions. The larvae were mounted on slides and their muscles were examined [43].

2.5 Component of the non-linear tensor susceptibility

Considering the propagation along the Z axis in the laboratory frame (X, Y, Z), the SHG response of myosin, due to the C_6 symmetry, is described by the three independent components $d_{11} = \chi^{(2)}_{XXX}$, $d_{12} = \chi^{(2)}_{Xii}$ and $d_{26} = \chi^{(2)}_{iiX} = \chi^{(2)}_{iXi}$, i = Y or Z (or Eq. (4)). In an equivalent way, these components are sometimes referred as d_{33}, d_{31} and d_{15} when inverting

Biomedical Optics EXPRESS

the myosin filament axis and the propagation one. The ratio $d_{11}/ d_{26} = 0.6$ is weaker than d_{12}/ d_{26}, which is close to unity [44]. To have maximum signal, the polarization of the exciting field must then be at 45° of the X and Y axis, in particular at 45° of the myosin filament axis X [44].

$$\begin{bmatrix} P_X^{2\omega} \\ P_Y^{2\omega} \\ P_Z^{2\omega} \end{bmatrix} = \begin{bmatrix} d_{11} & d_{12} & d_{12} & 0 & 0 & 0 \\ 0 & 0 & 0 & 0 & 0 & d_{26} \\ 0 & 0 & 0 & 0 & d_{26} & 0 \end{bmatrix} \begin{bmatrix} E_X^2 \\ E_Y^2 \\ E_Z^2 \\ 2E_Y E_Z \\ 2E_X E_Z \\ 2E_X E_Y \end{bmatrix} \quad (4)$$

For the PPLN, the $\chi^{(2)}$ of LiNbO3 has three independent components due to its 3m crystal class [45] such that its nonlinear susceptibility tensor writes in our coordinates:

$$\begin{bmatrix} 0 & 0 & 0 & 0 & d_{31} & -d_{22} \\ -d_{22} & d_{22} & 0 & d_{31} & 0 & 0 \\ d_{31} & d_{31} & d_{33} & 0 & 0 & 0 \end{bmatrix} \quad (5)$$

When the PPLN is used for quasi-phase matching, the polarization of light is usually set parallel to the Z-axis (the e-axis of the crystal) to access the highest nonlinear components of the $\chi^{(2)}$ (d_{33} and d_{31}). Here, in order to image the domains the propagation of light is set parallel to the Y-axis (see Fig. 1), such that the main excited component is d_{22} (see [46]). The components d_{33} and d_{31} are not excited in the scalar-field approximation, but can contribute due to the distortion of the polarization of the exciting beam occurring at tight focusing regimes according to the vectorial field model [47].

2.6 Numerical simulations

The numerical simulations are all performed using the Green's function approach (as in [20]), with a wavelength of 810nm, a waist of 0.7µm (meaning a spot size of 1.4µm diameter), and an integration volume of 2.8x2.8x10µm^3. The collecting lens is assumed at 3 mm from the focal volume, with a numerical aperture of 0.8. It is worth noting that the Green's function calculation takes into account the tensorial nature of $\chi^{(2)}$ and a vectorial exciting field that becomes significant when focused by a microscope objective [47]. The light is collected in the far-field with a collecting lens with an NA of 0.8 using a Monte Carlo integration with 5,000,000 points.

3. Results and discussion

3.1 Numerical simulations of the theoretical radiation pattern

First, numerical simulations were performed to compute the radiation pattern of the converted SHG signal observed before the collecting lens for two different cases: in the middle of a homogeneous $\chi^{(2)}$ zone (case I) and on an interface between two zones of opposite $\chi^{(2)}$ sign (case II), as indicated in Fig. 1(B). The radiation pattern is in the first case a standard 2D Gaussian (Fig. 2(A.I)) but at an interface it splits into two lobes that are π phase-shifted (Fig. 2(A.II)): in this case their amplitude is indeed of opposite sign. In the case (II) when the two lobes are recombined by a collecting lens (Fig. 2(B)), the detector can be positioned to have a complete (D2), partial (D1) or no (D3) overlap of the lobes on it. Position D1 implies complete destructive interference of both lobes and thus theoretically no signal. Position D3 is the other limit with no interference, such that the measured signal is the incoherent addition of

Biomedical Optics EXPRESS

both lobes. Finally, position D2 lays in between: the destructive interference of the lobes is only partial, such that some signal would be detected.

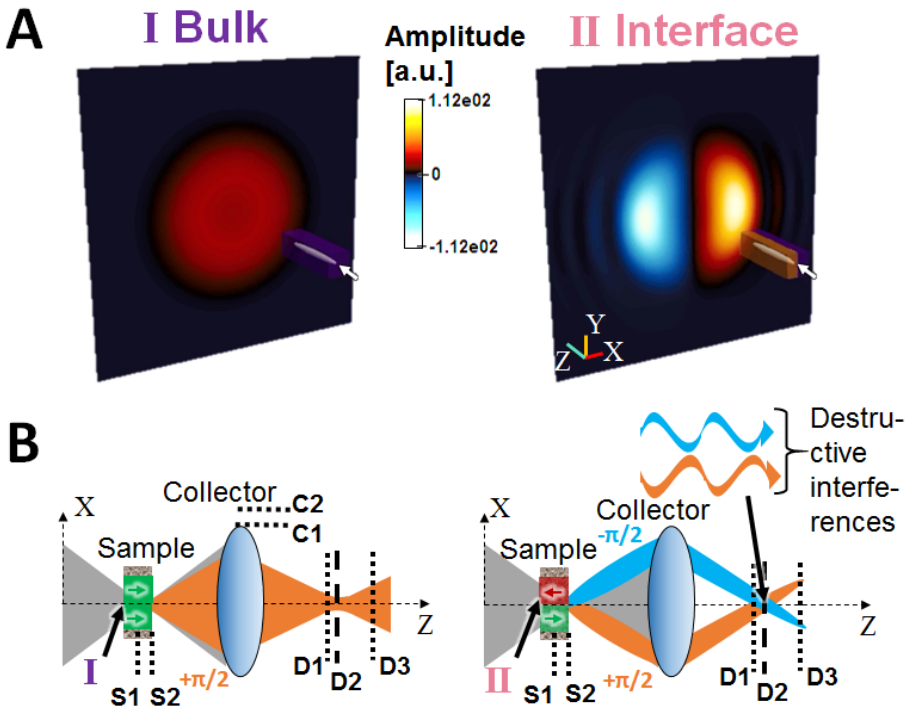

Fig. 2. Theoretical radiation pattern in different configurations of PPLN, and its consequences when being imaged on the detector. (A) Schematic view of the far-field SHG amplitude before the collector of a homogeneous medium and $\chi^{(2)}$ obtained by numerical simulations if the focal volume is located in the bulk (I, left), or if it is located at the interface between two domains with a $\chi^{(2)}$ of opposite sign (II, right). The focal volume is represented by a white oval (pointed by a white arrow), and the far-field pattern is here purposely moved very close to the excitation for the clarity of the illustration (not at scale). For the bulk (I) the shape is a standard 2D Gaussian whereas for the interface (II), the amplitude is spread over two side-lobes of opposite sign, which means their phases are π-phase-shifted. (B) Schematic view of the SH radiation pattern generation and its recombination on the detector by the collector, for the focal volume of excitation being in the bulk (left, I in green) or at an interface between two opposite polarities (right, II, in red and green). The excitation beam is shown in grey, and produces a Gaussian radiation pattern (orange) in case I (left), but two π-phase-shifted lobes (blue and orange) for case II (right). Their respective phases are indicated (-π/2 and π/2). Their subsequent collection leads to a recombination on the detector, which implies a partial (position D1) or total (position D2) overlap of the lobes, or no overlap at all (position D3) depending on the detector position. Since the lobes are π phase-shifted, their overlap will produce partial or complete destructive interference, as indicated by the two out-of-phase sine waves at the top of B. The different focus positions along the sample depth (Z) are indicated by S1 and S2 planes. Also, the collector might be well-aligned with its top at position C1, or misaligned at position C2. The off-axis angle of the lobes on B.II is purposely exaggerated for clarity.

The numerical simulations predict that the total integrated intensity - i.e. the signal measured by the detector during an experiment – is indeed 0 when the lobes overlap in case II (interface, detector at D2) because of destructive interferences. If the detector is misaligned in Z (position D3) such that the two lobes do not overlap at all, they would just sum up incoherently. In this case, the relative intensity is equal to 70% of the intensity detected from bulk (case I), i.e. a ratio $r_1 = 0.7:1$.

Biomedical Optics EXPRESS

Overall, the total intensity detected at the interface of the $\chi^{(2)}$ boundaries (II) is always smaller than the one detected in the bulk (I). For further information on the radiation pattern along the transition from the bulk (case I) to the interface (case II), we refer to the videos Visualization 1 and Visualization 2 in the supplementary material. They show numerical simulations of the amplitude of the SHG radiation pattern converted respectively at the surface (position S2 in Fig. 2(B)) or at a depth of Z = 5µm (position S1 in Fig. 2(B)). These two different sample positions S1 and S2 (Fig. 2(B)) also give similar radiation patterns for the interface, and a doughnut-shaped pattern (as already discussed in the literature [16]) is obtained if the excitation is Z = 5µm in depth, unlike the 2D Gaussian obtained when interacting with bulk at its surface. The intensities at Z = 5µm depth also conserve the ratio r_1 = 0.7:1 (see the 2D plots in the videos). Furthermore, the intensity ratios are conserved even with a large misalignment of the collecting lens in lateral position X (see Fig. 5 in the Appendix). If this misalignment is larger than 2mm, the signal decreases because the SHG beams are no longer reaching the detector. This is unrealistic to happen experimentally, as the collecting objective is aligned by maximizing the detected signal with a precision below 1mm. The different normalized integrated intensities of second harmonic signal obtained in the different configurations are summarized in the upper part of Table 1.

Table 1. Intensities at the detector in the bulk or at interfaces obtained by numerical simulations for the different configurations, and their comparison with the experimental values obtained in PPLN.

	Bulk	Interface
Complete overlap of the lobes on the detector	1	0
No overlap of the lobes on the detector	1	0.7
Experiment (PPLN, iris open)	1	2.1
Experiment (PPLN, iris closed to 5mm)	1	0.83

Interestingly, in Fig. 2(A), the individual peak amplitudes of both lobes are much higher than the one of the bulk due to the symmetry breaking, even though the integrated intensity over both lobes is smaller than in the case of the bulk. This can be understood by the absence of signal between the two lobes, and because the pattern associated with the two lobes concentrates the signal in two separated and smaller areas. The bulk pattern on the other hand is spread homogeneously over the whole disk (blue and orange regions in Fig. 2(A)), resulting in a higher number of photons spread over a larger zone.

Furthermore, these simulations have been adapted to the case of myosin and predict a radiation pattern that has the same shape, angle of emission, and relative amplitudes as for PPLN even though they have different $\chi^{(2)}$ symmetry tensors and coefficients. Thus, these results suggest that it is the geometrical property of the interface or the bulk that defines the radiation pattern.

3.2 PPLN: removing incoherent imaging artifacts

On the SHG images of PPLN, stripes occur at the interfaces (bright in Fig. 3(a) and dark for b, c and d) whose spatial thickness is approximately 1µm. This thickness is in good agreement with the expected lateral resolution of ~1µm as mentioned in the method section. The bright stripes in Fig. 3(a) offset the dynamic range of the image as they are 2.1 times higher than the signal in the homogeneous zones of the bulk and thus prevent a good visualization of the structure. This ratio is obtained by taking the average signal from the bright zones divided by the one of the homogeneous zones. Also, the bright stripes in Fig. 3(a) decrease from right to left due to a slight tilt of the sample along Z. It is not the case in the I-SHG image Fig. 3(c)

Biomedical Optics EXPRESS

because I-SHG results from a relative measurement that cancels such an effect. This cancellation is discussed mathematically in Eqs. (1) and (2).

We have discussed in section 3.1 the two limit cases of the effect of the detector position along Z, which show that the detected signal at the interface can theoretically vary between 0 (case D2 in Fig. 2(B.II)) and 0.7 times (case D3 in Fig. 2(B.II)) the signal detected in the bulk (see Table 1). The case in-between (D1 in Fig. 2(B)) corresponds to an experimentally realistic case since a perfect alignment is rarely achieved. Overall, the 2.1 times higher SH signal observed at the interfaces of PPLN in Fig. 3(a) cannot be explained by our numerical simulations, and we suspect that this stronger signal originates from additional sources such as the numerous imperfections and defects present at the involved $\chi^{(2)}$ boundaries, as mentioned before. In other words, these boundaries between two antiparallel noncentrosymmetric domains present strains and perturbations of the refractive index. Additionally, these imperfections are randomly positioned and if they are limited to the nanoscale, they will produce a local-field enhancement as described in [48–50]. This enhancement can be up to 10 times or more [51,52] and leads to "hotspots" that have already been observed even in centrosymmetric materials that present local defects [53]. The emission directionality of these hotspots is not as well-defined as for a conventional SHG signal emitted from an ordered structure, so they are detected as a scattering contribution at the detector. Hence, we expect that this SH signal exhibits a randomly-distributed phase at the detector according to the relation $\varphi = 2\pi L/\lambda$ where L is the optical path and λ is the wavelength. We emphasize that while the SH signal is 2.1 times higher at the interfaces of PPLN compared to the homogeneous zones, the corresponding interferometric contrast is 2.6 times lower (see Fig. 3(c)). This confirms that a significant fraction of the SH signal from the interfaces has a random phase.

To block this undesired intense contribution, an iris in the detection path was closed down to 5 mm, which defines the filtered SHG signal. This iris is positioned close to the imaging plane. However, we found that its precise axial position (Z) is non critical to remove the undesired intense contribution. In this condition, the filtered SHG signal is lower at the interfaces due to destructive interferences as expected from lobes of opposite polarities and predicted by the numerical simulations. More precisely, this SHG signal is reduced by 16% compared to the homogeneous zones (Fig. 3(c)). It is worth noting that closing the iris has no effect on the coherent signal from the homogeneous zones, thus rejecting exclusively the artefactual part. This can be seen on the grey profile plots of Fig. 3(e), as expected since the closed iris diameter is 5mm and the scanned region is only a few tens of μm^2, such that it rejects only the highly scattered part of the signal. This was further verified by measuring the SHG signal from a quartz plate under the same experimental conditions.

Interestingly, despite the fact that the interfaces appear as homogeneous signal stripes on the images, they actually correspond to a spatial average of the signal emitted by the numerous defects whose dimensions are at the nanoscale.

Using I-SHG, we show that there is no real difference in the interferometric contrast γ between the cases when the scattering is rejected or not (Fig. 3(b) and (d). On Fig. 3(e) the profile plots reveal that the case with the iris closed (black dashed line) has slightly less signal in the homogeneous part, and that for both open and closed iris (black continuous and dashed lines) the dip at the interfaces is deeper than in the case of SHG with iris closed (grey dashed line, filtered SHG). We also define the visibility of a certain feature in the image as:

$$Visibility = \frac{I_{max} - I_{min}}{I_{max} + I_{min}} \tag{6}$$

0 meaning no visibility and 1 a perfect one. The visibility of the interfaces in I-SHG is of 0.43 compared to 0.09 for the filtered SHG (iris closed). I-SHG thus enhances this visibility 5 times compared to filtered SHG.

Biomedical Optics EXPRESS

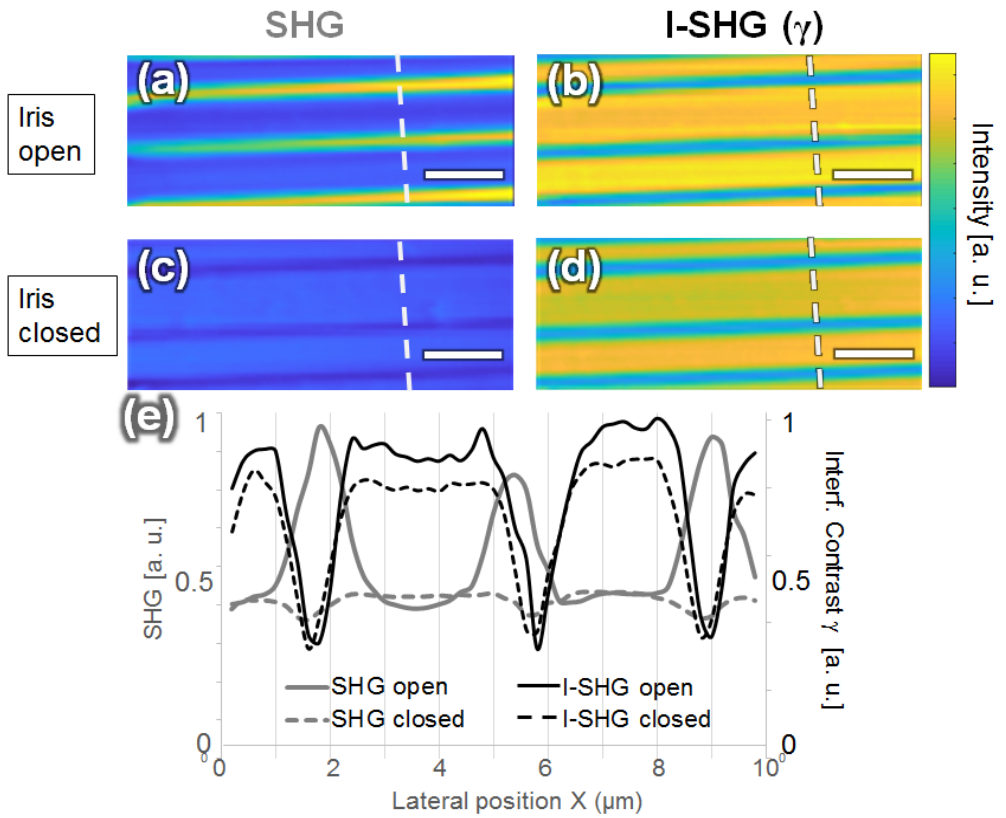

Fig. 3. (Left) Intensity SHG images of PPLN domains, where scattering occurs at the interfaces (a), compared to the same zone imaged with the scattering at the interfaces blocked by an iris (c). (Right) Interferometric contrast γ measured by I-SHG ((b) and (d)) of the same zone and under the same conditions and with same dynamic range as before. No clear differences are visible between these two I-SHG contrast images, showing that the scattering at the interfaces is averaged out by I-SHG. Scale-bars: 5μm. (e) Profile plots along the white dashed lines of the images. With the iris open (grey continuous line), there are intense contributions at the interfaces between domains, which are two times more intense than the homogeneous zones. Closing the iris rejects these contributions and reveals the little dips in SHG signal at the interfaces (grey dashed line) corresponding to destructive interferences (16% lower than the homogeneous contribution), while maintaining the same level of signal for the homogeneous parts. The I-SHG contrast γ is very similar in both cases of open (black continuous line) and closed iris (black dashed line). In the homogeneous zones the closed case has only 10% less signal than the open case. With I-SHG, the interfaces exhibit a high contrast, with a signal drop of more than 50% when going from the homogeneous zones to the interfaces.

These I-SHG images confirm that the very intense SH signal at the interfaces does indeed not exhibit a well-defined phase and thus cannot interfere with the reference beam, and importantly that I-SHG is therefore able to remove this incoherent signal that only acts as a contribution to the background. The imperfect interface in PPLN can thus directly be revealed in I-SHG, while it requires spatial filtering in standard SHG to remove the bright and artefactual interface signal.

3.3 Myosin: removing coherent imaging artifacts

In zebrafish skeletal muscle, similar interfaces as in PPLN are present but they lead to different artifacts: while in all cases alternating structures are present in the samples, they were only sometimes visible as double structures in conventional SHG microscopy. In other cases, the myosin interfaces could not be observed with standard SHG. To begin with, we

Biomedical Optics EXPRESS

present here an SHG image of the sarcomeres from muscles of zebrafish, where the observed patterns are double-band (as mentioned earlier, see Fig. 1(B)). The adjacent sarcomeres appear separated by the I-bands (white arrow-heads in images of Fig. 4) where the SHG signal is minimum, within whom the A-band is split in two by the M-line (where the opposite myosin ends overlap, brown arrows of Fig. 4). This occurs as a dip in SHG signal with slightly more signal than in the I-band (see Fig. 4(a)).

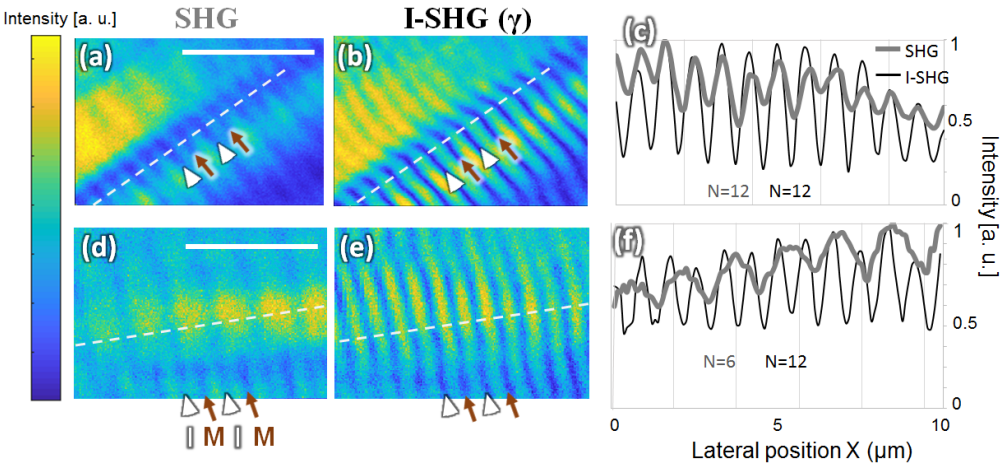

Fig. 4. Myosin inside sarcomeres of skeletal muscle of zebrafish imaged by SHG (left column) and I-SHG (middle column). The I-SHG interferometric contrast enhances the visibility of the myosin pattern compared to the intensity SHG. (a) SHG intensity in 6-months-old zebrafish muscle, showing the expected double-band patterns of myosin. The I-SHG interferometric contrast γ (middle) of the same zones (b) exhibits an enhanced visibility of the sarcomeres pattern compared to the intensity SHG. This is better observed when plotting an intensity projection (right) along the white dashed lines: the visibility of the oscillations is enhanced from 2.5 to 4 times (depending on the zone) for I-SHG (black lines in (c)) compared to SHG (grey lines). (d-f) Same as before, in a larvae zebrafish: the selected zones show a single-band pattern of myosin in intensity SHG (d), while the corresponding interferometric contrast γ in I-SHG (e) reveals the double-band pattern. (f) Profile plots of signals along the white dashed line shown on the images: there are indeed twice the number of peaks for the I-SHG compared to the SHG case, whereas for (a) and (b) their number is similar. Two I-band positions are spotted in each image by white arrow-heads, and two M-lines by brown arrows. Equivalent exposure time is 400μs and 100μs per pixel for the SHG images and I-SHG images, respectively. For SHG images the dynamic range of display is enhanced compared to I-SHG, for clarity. Scale-bars = 5μm for all the images.

When the interferometric contrast γ is measured (by I-SHG), these sarcomeres are revealed more clearly (Fig. 4(b)): the visibility of the "oscillations" (alternation of bulk/interface) is of 0.7 compared to 0.2 for the intensity SHG images (see Fig. 4(c)), so 3 times higher. Interferometric SHG thus greatly enhances the visibility (or imaging contrast) compared to standard intensity SHG. It should be noted that all these images of myosin show no difference whether the iris mentioned earlier was open or closed, because there is no highly scattered SH signal present.

We then show another standard SHG image where the double-band pattern is artifactly hidden in some areas (Fig. 4(d)). Only the I-SHG interferometric contrast γ can reveal it (Fig. 4(e)). On the profile plots (Fig. 4(f)) there are clearly twice the number of dips in the I-SHG signal compared to the SHG one. In the bottom of the image, the double-band pattern is still visible in standard intensity SHG, which shows that this imaging artifact does not occur equally everywhere. It is strongly dependent on the interferences between the SHG converters, and thus on their spatial arrangement. Indeed, the 3D stacking of sarcomeres in muscle can imply artifacts in the axial direction due to the Gouy phase-shift, for some areas in the sample where the sarcomeres' spacing matches a certain phase relation [26]. For example,

Biomedical Optics EXPRESS

in the lateral plane (i.e. XY in Fig. 1(B)) plane, the proximity of shifted sarcomeres in the focal area can result in an SHG signal with similar artefactual connections between the sarcomeres (i.e. a single-band pattern), as extensively discussed before [25,26]. Lastly, the propagation of the SHG wave through the thickness of the muscle (several μm), that is a stacking of sarcomeres, can also be a source of varying phase retardation and thus artifacts in the acquired SHG images. While the detailed origin of the coherent imaging artifacts occurring in the myosin of muscle in conventional SHG microscopy is still under debate, it is assumed that it results from coherent built-up of the SHG signal in a highly complex tissue [25,26]. This is different from the I-SHG case, where the SHG radiation interferes with the reference beam and the I-SHG contrast γ reveals the highest phase modulation. This I-SHG contrast appears to be lower at the M-line than elsewhere in the myosin filament, and thus reveals the destructive interferences occurring at the M-line and uncovers the double-band patterns. Therefore, I-SHG allows to remove a typically observed imaging artifact for such structures, namely the single-band pattern.

3.4 Comparison between PPLN and myosin I-SHG imaging

I-SHG was already used to advance standard SHG microscopy as mentioned in the introduction. Here we focus on the additional advantage of I-SHG being capable of eliminating two different types of imaging artifacts – coherent and incoherent ones.

The converted SHG inside a sample can in general be written as [54]: $I_{SH} = I_{SH}^{ballist} + I_{SH}^{scatter}$, where $I_{SH}^{ballist}$ is the main contribution which has experienced little to no scattering. This conserves the phase relation and thus its coherence. In the case of our example myosin, $I_{SH}^{ballist}$ represents the observed SHG signal. In contrast, the term $I_{SH}^{scatter}$ preserves no coherence and is usually much smaller than the ballistic one. An exception are structures with many randomly-oriented nano-emitters like the PPLN interfaces of our first example, which leads to incoherent imaging artifacts. I-SHG averages this contribution out, as it is an interferometry technique that reveals only the coherent interfering part.

Table 2 summarizes the comparison between PPLN and myosin materials, pointing out the similarity of the expected effects on the SHG at the interfaces and the differences of the artifacts that occur at these interfaces: these structures are analogous, except that the nature of the imaging artifacts is incoherent for PPLN, and coherent for myosin. There are no coherent imaging artifacts in PPLN because, unlike muscle, there is no 3D arrangement of many domains with opposite polarity, but rather a single and well-ordered periodicity, homogeneous in the axial direction (along Z).

Both coherent and incoherent artifacts are fully eliminated in I-SHG microscopy, however in different ways. Coherent artifacts remain visible in the optically collected interferograms but are eliminated in the subsequent image processing (see Fig. 6 of the Appendix, bottom). Incoherent artifacts, on the other hand, already do not show up in the measured interferograms as they only contribute as a constant background for every phase-shift (see Fig. 6, top). Table 2 also points out the two major advantages of I-SHG: it is capable of totally removing artefactual interface structures that appear in some cases in conventional SHG. And even if no artifacts occur, such that structures are correctly imaged by SHG microscopy, the I-SHG technique further increases the visibility of these interfaces by a factor of 3 (in myosin) to 5 (in PPLN). The ability of I-SHG to increase this visibility relies on a reference SHG beam with a well-defined phase. For thick tissues, because of scattering, such phase definition might be partially lost. Yet, this will only reduce the interferometric contrast, so that a phase-modulation could still be extracted to measure the relative polarity of structures.

Biomedical Optics EXPRESS

Table 2. Summary of the differences and similarities between the two samples under study.

	PPLN	Myosin
Periodic domains of opposite polarity	**Yes**	**Yes**
Organization of domains	Single periodic structure	Complex arrangement of multiple periodic structures
Number of interface types	1 with opposite polarities	2 (1 with opposite polarities, 1 without SHG converter)
At interfaces, SHG radiation pattern presents two lobes that interfere destructively, leading to minimum signal	**Yes**	**Yes**
Incoherent signal contribution/artifacts	**Yes**	**No**
SHG ratio at interface/bulk due to hotspots	**× 2.1**	**No hotspots**
Need for iris filtering in standard SHG	**Yes**	**No**
Coherent imaging artifacts in SHG	**No**	**In some cases**
Imaging artifacts removed in I-SHG	**Yes**	**Yes**
Increase of visibility of boundaries by I-SHG	**× 5**	**× 3**

4. Conclusion

The interface between two $\chi^{(2)}$ of opposite polarity leads to an SHG radiation pattern with two lobes whose relative phase is π phase-shifted, which is elucidated in detail by numerical simulations. These lobes normally lead to destructive interferences when being recombined on a detector. However, in some cases of standard SHG, a signal occurs at these interfaces for two different reasons: first, in PPLN the signal is given by an incoherent hotspot contribution due to imperfections, which can be eliminated by optical filtering. Second, in muscle sarcomeres, the signal at these interfaces can produce imaging artifacts due to the coherent nature of the SHG light, which are insensitive to optical filtering. For both examples, it is shown that I-SHG fully eliminates these artifacts, and reveals the destructive interferences at the interfaces without the need of any further processing like spatial filtering. Furthermore, I-SHG even allows to increase the visibility of the interfaces by a factor of 3 to 5. This is of great importance for interpreting correctly the SHG signal produced in various materials, especially in complex biological tissues.

Funding

M.P., F.L. and S.P acknowledges Canada Foundation for Innovation (CFI) and the Natural Sciences and Engineering Research Council of Canada (NSERC). M.P. acknowledges financial support from the NSERC CREATE/GRK program. M.S. acknowledges financial support from the Ecole Doctorale Interface, Univ. Paris-Saclay.

Disclosures

The authors declare that there are no conflicts of interest related to this article.

Biomedical Optics EXPRESS

Appendix: additional numerical simulations

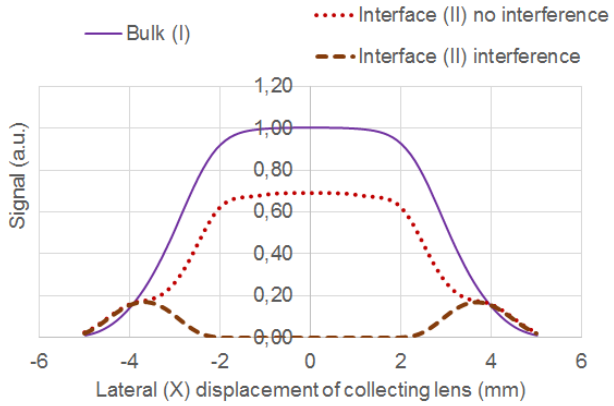

Fig. 5. Numerical simulations of the intensities at the detector when the excitation is in the bulk (I, violet continuous line) or at the interfaces of opposite polarities (II, light and dark red dashed line). The intensity at the interface is 0 when the lobes fully destructively interfere (dark red dashed line), but of 0.7 when they do not overlap on the detector so that there is no interference (light red dotted). In comparison, the intensity for the bulk is 1. These ratios remain the same if the lateral misalignment in X of the collecting objective is below 2 mm. If this misalignment goes over 2 mm, the signal for the bulk and for the interface with no interference decrease as the SHG beams go progressively outside the detector. For the case where the lobes overlap, at high lateral misalignment, the lens does not progressively capture one of the lobes so that the destructive interferences can only partially occur such that the intensity is larger than 0. Over 4 mm of misalignment, all signals decrease to 0. The detector is 45mm^2 placed at 3.3 mm of the collecting lens, whose equivalent diameter is 8 mm.

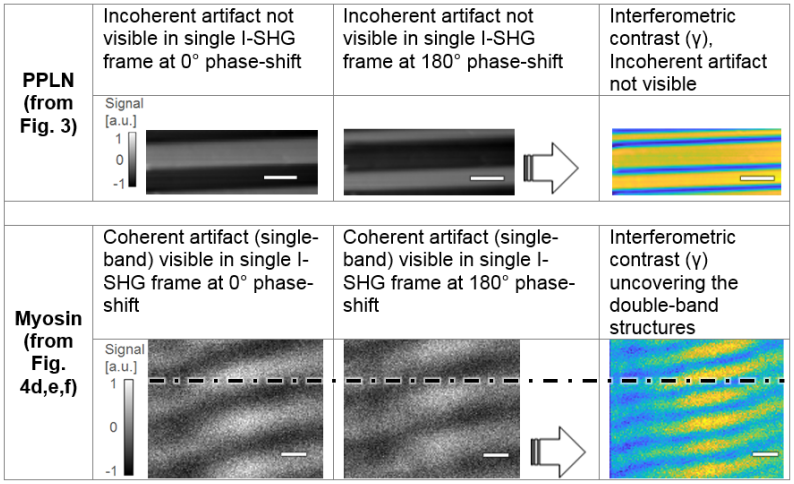

Fig. 6: Comparison of the incoherent and coherent artifacts removal by I-SHG. (Top) PPLN images of Fig. 3, showing the I-SHG contrast γ (right) and two interferograms at 0° (left) and 180° (middle) used to reconstruct the I-SHG image. The incoherent artifacts (bright stripes) are removed from the interferograms directly. Scale-bar: 5μm. (Bottom) Same with myosin images from Fig. 4(e). The coherent artifacts (single-band pattern) are still visible on interferograms (left and middle), but these one are indeed π phase-shifted. The double-band pattern is revealed only in the I-SHG contrast γ (right). A dashed black line guides the eye for comparison between images. Scale-bar: 1μm.

Biomedical Optics EXPRESS

References

1. S. Roth and I. Freund, "Optical second-harmonic scattering in rat-tail tendon," Biopolymers **20**(6), 1271–1290 (1981).
2. P. J. Campagnola, A. C. Millard, M. Terasaki, P. E. Hoppe, C. J. Malone, and W. A. Mohler, "Three-dimensional high-resolution second-harmonic generation imaging of endogenous structural proteins in biological tissues," Biophys. J. **82**(1 Pt 1), 493–508 (2002).
3. A. Zoumi, A. Yeh, and B. J. Tromberg, "Imaging cells and extracellular matrix in vivo by using second-harmonic generation and two-photon excited fluorescence," Proc. Natl. Acad. Sci. U.S.A. **99**(17), 11014–11019 (2002).
4. W. Denk, J. H. Strickler, and W. W. Webb, "Two-photon laser scanning fluorescence microscopy," Science **248**(4951), 73–76 (1990).
5. F. Helmchen and W. Denk, "Deep tissue two-photon microscopy," Nat. Methods **2**(12), 932–940 (2005).
6. P. J. Campagnola and L. M. Loew, "Second-harmonic imaging microscopy for visualizing biomolecular arrays in cells, tissues and organisms," Nat. Biotechnol. **21**(11), 1356–1360 (2003).
7. S. Bancelin, C. Aimé, I. Gusachenko, L. Kowalczuk, G. Latour, T. Coradin, and M.-C. Schanne-Klein, "Determination of collagen fibril size via absolute measurements of second-harmonic generation signals," Nat. Commun. **5**(1), 4920 (2014).
8. A. K. Dunn, V. P. Wallace, M. Coleno, M. W. Berns, and B. J. Tromberg, "Influence of optical properties on two-photon fluorescence imaging in turbid samples," Appl. Opt. **39**(7), 1194–1201 (2000).
9. W. R. Zipfel, R. M. Williams, R. Christie, A. Y. Nikitin, B. T. Hyman, and W. W. Webb, "Live tissue intrinsic emission microscopy using multiphoton-excited native fluorescence and second harmonic generation," Proc. Natl. Acad. Sci. U.S.A. **100**(12), 7075–7080 (2003).
10. A. E. Tuer, M. K. Akens, S. Krouglov, D. Sandkuijl, B. C. Wilson, C. M. Whyne, and V. Barzda, "Hierarchical model of fibrillar collagen organization for interpreting the second-order susceptibility tensors in biological tissue," Biophys. J. **103**(10), 2093–2105 (2012).
11. I. Gusachenko, V. Tran, Y. Goulam Houssen, J. M. Allain, and M.-C. Schanne-Klein, "Polarization-resolved second-harmonic generation in tendon upon mechanical stretching," Biophys. J. **102**(9), 2220–2229 (2012).
12. C. P. Brown, M. A. Houle, M. Chen, A. J. Price, F. Légaré, and H. S. Gill, "Damage initiation and progression in the cartilage surface probed by nonlinear optical microscopy," J. Mech. Behav. Biomed. Mater. **5**(1), 62–70 (2012).
13. S. V. Plotnikov, A. C. Millard, P. J. Campagnola, and W. A. Mohler, "Characterization of the myosin-based source for second-harmonic generation from muscle sarcomeres," Biophys. J. **90**(2), 693–703 (2006).
14. V. Nucciotti, C. Stringari, L. Sacconi, F. Vanzi, L. Fusi, M. Linari, G. Piazzesi, V. Lombardi, and F. S. Pavone, "Probing myosin structural conformation in vivo by second-harmonic generation microscopy," Proc. Natl. Acad. Sci. U.S.A. **107**(17), 7763–7768 (2010).
15. N. Olivier, M. A. Luengo-Oroz, L. Duloquin, E. Faure, T. Savy, I. Veilleux, X. Solinas, D. Débarre, P. Bourgine, A. Santos, N. Peyriéras, and E. Beaurepaire, "Cell Lineage Reconstruction of Early Zebrafish Embryos Using Label-Free Nonlinear Microscopy," Science **329**(5994), 967–971 (2010).
16. M. Rivard, M. Laliberté, A. Bertrand-Grenier, C. Harnagea, C. P. Pfeffer, M. Vallières, Y. St-Pierre, A. Pignolet, M. A. El Khakani, and F. Légaré, "The structural origin of second harmonic generation in fascia," Biomed. Opt. Express **2**(1), 26–36 (2011).
17. R. Lacomb, O. Nadiarnykh, S. S. Townsend, and P. J. Campagnola, "Phase matching considerations in second harmonic generation from tissues: Effects on emission directionality, conversion efficiency and observed morphology," Opt. Commun. **281**(7), 1823–1832 (2008).
18. S. Yazdanfar, L. Laiho, and P. So, "Interferometric second harmonic generation microscopy," Opt. Express **12**(12), 2739–2745 (2004).
19. M. Rivard, C.-A. Couture, A. K. Miri, M. Laliberté, A. Bertrand-Grenier, L. Mongeau, and F. Légaré, "Imaging the bipolarity of myosin filaments with Interferometric Second Harmonic Generation microscopy," Biomed. Opt. Express **4**(10), 2078–2086 (2013).
20. M. Rivard, K. Popov, C. A. Couture, M. Laliberté, A. Bertrand-Grenier, F. Martin, H. Pépin, C. P. Pfeffer, C. Brown, L. Ramunno, and F. Légaré, "Imaging the noncentrosymmetric structural organization of tendon with Interferometric Second Harmonic Generation microscopy," J. Biophotonics **7**(8), 638–646 (2014).
21. C. A. Couture, S. Bancelin, J. Van der Kolk, K. Popov, M. Rivard, K. Légaré, G. Martel, H. Richard, C. Brown, S. Laverty, L. Ramunno, and F. Légaré, "The Impact of Collagen Fibril Polarity on Second Harmonic Generation Microscopy," Biophys. J. **109**(12), 2501–2510 (2015).
22. S. Bancelin, C.-A. Couture, M. Pinsard, M. Rivard, P. Drapeau, and F. Légaré, "Probing microtubules polarity in mitotic spindles in situ using Interferometric Second Harmonic Generation Microscopy," Sci. Rep. **7**(1), 6758 (2017).
23. S. Bancelin, C.-A. C.-A. Couture, K. Légaré, M. Pinsard, M. Rivard, C. Brown, and F. Légaré, "Fast interferometric second harmonic generation microscopy," Biomed. Opt. Express **7**(2), 399–408 (2016).
24. R. W. Boyd, "The Nonlinear Optical Susceptibility," in *Nonlinear Optics, 3rd Edition* (Academic Press, 2008), pp. 3–51.
25. D. Rouède, J.-J. Bellanger, G. Recher, and F. Tiaho, "Study of the effect of myofibrillar misalignment on the sarcomeric SHG intensity pattern," Opt. Express **21**(9), 11404–11414 (2013).

Biomedical Optics EXPRESS

26. W. P. Dempsey, N. O. Hodas, A. Ponti, and P. Pantazis, "Determination of the source of SHG verniers in zebrafish skeletal muscle," Sci. Rep. **5**(1), 18119 (2015).
27. D. Irzhak, D. Roshchupkin, and L. Kokhanchik, "X-ray diffraction on a LiNbO3 crystal with a short period regular domain structure," Ferroelectrics **391**(1 PART 3), 37–41 (2009).
28. V. Gopalan, V. Dierolf, and D. A. Scrymgeour, "Defect–Domain Wall Interactions in Trigonal Ferroelectrics," Annu. Rev. Mater. Res. **37**(1), 449–489 (2007).
29. S. Helmfrid, G. Arvidsson, and J. Webjörn, "Influence of various imperfections on the conversion efficiency of second-harmonic generation in quasi-phase-matching lithium niobate waveguides," J. Opt. Soc. Am. B **10**(2), 222 (1993).
30. F. Zernike and J. E. Midwinter, "4.5 Lithium Niobate," in *Applied Nonlinear Optics* (Wiley Interscience, 1973), pp. 87–88.
31. M. Neradovskiy, E. Neradovskaia, D. Chezganov, E. Vlasov, V. Y. V. Y. A. Shur, H. Tronche, F. Doutre, G. Ayenew, P. Baldi, M. De Micheli, and C. Montes, "Second harmonic generation in periodically poled lithium niobate waveguides with stitching errors," J. Opt. Soc. Am. B **35**(2), 331 (2018).
32. D. Rouède, J.-J. Bellanger, E. Schaub, G. Recher, and F. Tiaho, "Theoretical and experimental SHG angular intensity patterns from healthy and proteolysed muscles," Biophys. J. **104**(9), 1959–1968 (2013).
33. G. Recher, D. Rouède, P. Richard, A. Simon, J.-J. Bellanger, and F. Tiaho, "Three distinct sarcomeric patterns of skeletal muscle revealed by SHG and TPEF microscopy," Opt. Express **17**(22), 19763–19777 (2009).
34. T. Boulesteix, E. Beaurepaire, M.-P. Sauviat, and M.-C. Schanne-Klein, "Second-harmonic microscopy of unstained living cardiac myocytes: measurements of sarcomere length with 20-nm accuracy," Opt. Lett. **29**(17), 2031–2033 (2004).
35. M. Both, M. Vogel, O. Friedrich, F. von Wegner, T. Künsting, R. H. A. Fink, and D. Uttenweiler, "Second harmonic imaging of intrinsic signals in muscle fibers in situ," J. Biomed. Opt. **9**(5), 882–892 (2004).
36. O. Friedrich, M. Both, C. Weber, S. Schürmann, M. D. H. Teichmann, F. von Wegner, R. H. A. Fink, M. Vogel, J. S. Chamberlain, and C. Garbe, "Microarchitecture is severely compromised but motor protein function is preserved in dystrophic mdx skeletal muscle," Biophys. J. **98**(4), 606–616 (2010).
37. W. R. Zipfel, R. M. Williams, and W. W. Webb, "Nonlinear magic: Multiphoton microscopy in the biosciences," Nat. Biotechnol. **21**(11), 1369–1377 (2003).
38. J. Schindelin, I. Arganda-Carreras, E. Frise, V. Kaynig, M. Longair, T. Pietzsch, S. Preibisch, C. Rueden, S. Saalfeld, B. Schmid, J. Y. Tinevez, D. J. White, V. Hartenstein, K. Eliceiri, P. Tomancak, and A. Cardona, "Fiji: An open-source platform for biological-image analysis," Nat. Methods **9**(7), 676–682 (2012).
39. J. E. Greivenkamp, "Generalized data reduction for heterodyne interferometry," Opt. Eng. **23**(4), 350–352 (1984).
40. Z. Wang and B. Han, "Advanced iterative algorithm for phase extraction of randomly phase-shifted interferograms," Opt. Lett. **29**(14), 1671–1673 (2004).
41. R. Stolle, G. Marowsky, E. Schwarzberg, and G. Berkovic, "Phase measurements in nonlinear optics," Appl. Phys. B Laser Opt. **63**(5), 491–498 (1996).
42. T. Colomb, J. Kühn, F. Charrière, C. Depeursinge, P. Marquet, and N. Aspert, "Total aberrations compensation in digital holographic microscopy with a reference conjugated hologram," Opt. Express **14**(10), 4300–4306 (2006).
43. M. Westerfield, *The Zebrafish Book: A Guide for the Laboratory Use of Zebrafish (Danio rerio)* (Eugene University of Oregon Press, 2007).
44. F. Tiaho, G. Recher, and D. Rouède, "Estimation of helical angles of myosin and collagen by second harmonic generation imaging microscopy," Opt. Express **15**(19), 12286–12295 (2007).
45. R. W. Boyd, *Nonlinear Optics* (Academic Press, 2008), **2**(9).
46. M. Odstrcil, P. Baksh, C. Gawith, R. Vrcelj, J. G. Frey, and W. S. Brocklesby, "Nonlinear ptychographic coherent diffractive imaging," Opt. Express **24**(18), 20245–20252 (2016).
47. M. Gu, "Imaging with a High Numerical-Aperture Objective," in *Advanced Optical Imaging Theory* (Springer, 1999), pp. 155–165.
48. A. Bouhelier, M. Beversluis, A. Hartschuh, and L. Novotny, "Near-Field Second-Harmonic Generation Induced by Local Field Enhancement," Phys. Rev. Lett. **90**(1), 013903 (2003).
49. R. W. Boyd, "Local-Field Corrections to the Nonlinear Optical Susceptibility," in *Nonlinear Optics, 3rd Edition* (Academic Press, 2008), pp. 194–195.
50. T. Birr, T. Fischer, A. B. Evlyukhin, U. Zywietz, B. N. Chichkov, and C. Reinhardt, "Phase-Resolved Observation of the Gouy Phase Shift of Surface Plasmon Polaritons," ACS Photonics **4**(4), 905–908 (2017).
51. G. T. Boyd, T. Rasing, J. R. R. Leite, and Y. R. Shen, "Local-field enhancement on rough surfaces of metals, semimetals, and semiconductors with the use of optical second-harmonic generation," Phys. Rev. B Condens. Matter **30**(2), 519–526 (1984).
52. A. V. Zayats, T. Kalkbrenner, V. Sandoghdar, and J. Mlynek, "Second-harmonic generation from individual surface defects under local excitation," Phys. Rev. B Condens. Matter Mater. Phys. **61**(7), 4545–4548 (2000).
53. M. S. Yeganeh, J. Qi, A. G. Yodh, and M. C. Tamargo, "Influence of heterointerface atomic structure and defects on second-harmonic generation," Phys. Rev. Lett. **69**(24), 3579–3582 (1992).
54. J. Martini, V. Andresen, and D. Anselmetti, "Scattering suppression and confocal detection in multifocal multiphoton microscopy," J. Biomed. Opt. **12**(3), 034010 (2007).